Acta Astronautica 226 (2025) 791–802

Contents lists available at ScienceDirect

Acta Astronautica

journal homepage: www.elsevier.com/locate/actaastro

In-flight calibration of the MEDA-TIRS instrument onboard NASA's Mars2020 mission

Eduardo Sebastián [a,*], Germán Martínez [a,b], Miguel Ramos [c], Michael D. Smith [d], Verónica Peinado [a], Luis Mora [a], Mark T. Lemmon [e], Álvaro de Vicente-Retortillo [a], Javier de Lucas [f], Ricardo Ferrándiz [a], José A. Rodríguez-Manfredi [a]

[a] Departamento de Instrumentación Espacial, Centro de Astrobiología (CSIC-INTA), Torrejón de Ardoz, Madrid, Spain
[b] Lunar and Planetary Institute/USRA, Houston, TX, USA
[c] Departamento Física y Matemáticas, Universidad de Alcalá, Alcalá de Henares, Madrid, Spain
[d] NASA Goddard Space Flight Center, Greenbelt, MD, USA
[e] Space Science Institute, Boulder, CO, USA
[f] Instituto Nacional de Técnica Aeroespacial (INTA), Torrejón de Ardoz, Madrid, Spain

ARTICLE INFO

Keywords:
Mars
Mars 2020
Spacecraft IR radiometer
In-flight calibration
Detector modeling and algorithm
Calibration uncertainty

ABSTRACT

This article describes a novel procedure and algorithm used for the in-flight calibration of the Thermal Infrared Sensor (TIRS) onboard the Mars 2020 mission. The purpose is to recalibrate the responsivity of TIRS' IR detectors as they degrade following surface operations and exposure to harsh environmental conditions. Using data from in-flight calibration campaigns conducted through sol 800 of this mission, we report the time evolution of the responsivity for the different IR detectors, as well as the final performance achieved by the algorithm in the real operating environment. Moreover, we analyzed changes in responsivity as a function of TIRS geometric design and environmental factors, e.g., detector orientation, direct exposure to prevailing winds and solar radiation, electrostatic properties of the detector filter, and atmospheric dust concentration. We concluded that dust deposition on the detectors' filter during landing, and later during operation is the most likely cause of the degradation observed in the various channels, with gravitational sedimentation and the capacity of the filters to accumulate electrostatic charge being key factors. The relative and absolute degradation of the TIRS is similar to those reported by other Martian missions and instruments with similar orientations, and to date, it has shown no signs of cleaning after more than a year on the surface of Mars. Accounting for changes in responsivity during the mission is critical to maintaining the reliability of TIRS measurements, which will later be made available in NASA's Planetary Data System for the benefit of the scientific community.

1. Introduction

The Thermal InfraRed Sensor (TIRS) is one of the six environmental sensors comprising the Mars Environmental Dynamics Analyzer (MEDA) [1], which in turn is one of the seven scientific instruments onboard NASA's Mars2020 Perseverance rover [2]. The rover landed on Mars on February 18th, 2021, near the northwest rim of the Jezero crater (77.5945°E, 18.3628°N, −2656 m). Since that date, TIRS has been measuring the net thermal long wave (LW) infrared radiation at the surface using two pyrgeometers looking upward (channel IR1) and downward (channel IR4); the reflected short wave (SW) solar radiation at the surface using a downward-looking pyranometer (channel IR3); and the atmospheric (channel IR2) and surface skin temperatures (channel IR5). These measurements have allowed the characterization of key parameters for modeling the Martian atmosphere and its interaction with the planet's surface [3,4].

TIRS measurements are performed using five thermopiles as infrared transducers located at the TIRS sensor head (Fig. 1), operating in the wavelength bands, pointing angles, and field of view (FoV) described in Table 1. The TIRS electronics is located at the MEDA's Instrument Control Unit (ICU), which is accommodated inside the rover body away from the sensor head. A general description of the TIRS radiometer and a preliminary analysis of its performance was presented in Ref. [5]. The final design of the flight model and its performance are described in

* Corresponding author.
E-mail address: sebastianme@cab.inta-csic.es (E. Sebastián).

https://doi.org/10.1016/j.actaastro.2024.11.015
Received 8 January 2024; Received in revised form 6 November 2024; Accepted 7 November 2024
Available online 9 November 2024
0094-5765/© 2024 IAA. Published by Elsevier Ltd. All rights are reserved, including those for text and data mining, AI training, and similar technologies.

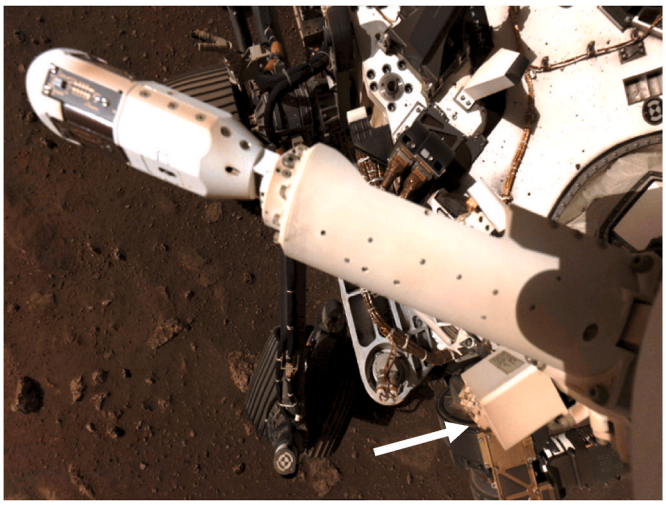


Fig. 1. The TIRS sensor head (white arrow) is located on the Remote Sensing Mast of Perseverance. This image was taken by the Navigation Cameras on Feb. 28, 2021 (credit NASA-JPL).

Table 1
Specification of TIRS.

Channel	Purpose	Spectral range	Pointing angles	Field of view (Vertical, Horizontal)
IR1	Downward long wave	6.5–30.0 μm	Upward (+35°)	±10°, ±20°
IR2	Air Temperature	14.5–15.5 μm	Upward (+35°)	±10°, ±20°
IR3	Upward short wave	0.3–3.0 μm	Downward (−35°)	±10°, ±20°
IR4	Upward long wave	6.5–30.0 μm	Downward (−35°)	±10°, ±20°
IR5	Ground Temperatue	8.0–14.0 μm	Downward (−35°)	±10°, ±20°

Ref. [1].

The responsivity of the TIRS IR detectors can be degraded throughout the mission by several factors, of which the following are considered to be the most important: (1) changes in the optical properties of the coating of the thermopile transducer element [6], (2) the loss of package hermeticity and the subsequent change of the thermal properties of the inner atmosphere [7], and (3) the deposition of dust on the thermopile's filter, modifying the outside viewing factor and the global responsivity of the sensor [8,9]. To correct for these effects, the TIRS incorporates an in-flight recalibration system [1,5].

The general structure, test divisions, objectives, and execution time frame of the TIRS calibration plan are shown in Fig. 2. The radiometric, angular, and thermal calibrations are described in detail in Refs. [10, 11]. In this article, we describe the last set of calibration tests devoted to the in-flight estimation of changes in the responsivity of the TIRS channels. Such tests consisted of calibration sequences for purely technical and non-scientific purposes, carried out during the first 800 sols (sol, name for a Martian day) of *Perseverance* surface operations.

A few radiometers similar to TIRS have been used for in-situ planetary exploration. Examples include the Multi-Purpose Sensors for Surface and Subsurface Science-Thermal Mapper (MUPUS-TM) onboard the Rosetta mission [12], the Rover Environmental Monitoring Station –Ground Temperature Sensor (REMS-GTS) pyrometer [8] onboard the *Curiosity* rover of the Mars Science Laboratory mission to Mars, and the Heat Flow and Physical Properties Package-Radiometer (HP^3-RAD) a radiometer onboard the InSight mission [13]. However, to the best of our knowledge, the results of in-flight calibrations during surface operations have only been published for the HP^3-RAD radiometer [9].

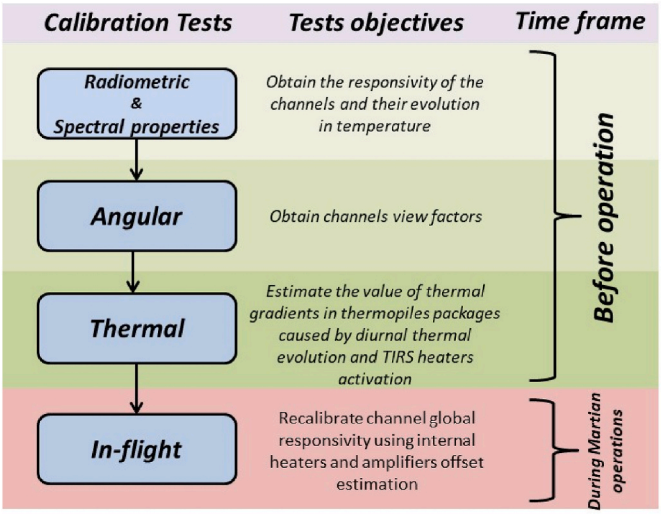


Fig. 2. General view of the TIRS calibration plan.

This article is structured as follows. Section 2 describes the in-flight calibration hardware and software, and the different calibration alternatives. Section 3 describes the mathematical modeling and the algorithm supporting the in-flight calibrations. Section 4 shows the results of the several calibration campaigns, carried out during the surface operations, as well as an analysis of the possible causes that justify the reported degradations. Finally, section 5 presents the main conclusions.

2. In-flight calibration system

The TIRS in-flight calibration system [5] uses support and calibration plate heaters to warm up the mechanical sub-assemblies (Fig. 3a). These are similar systems intended for the same purpose, that can act as a backup solution to each other, but with different operational procedures. The calibration plate is an element that partially blocks the field of view of the thermopiles. When heated, it increases the incoming radiative flux that is integrated by the thermopiles (Fig. 3b). This same design and operational procedure were already used in previous radiometers [8,9,12]. On the other hand, the support plate is the mechanical subassembly in which the thermopiles are accommodated, increasing the radiative flux leaving the thermopiles when heated (Fig. 3b). This calibration system is a novelty in the design of space radiometers. Both the support and calibration plate heaters can be driven independently.

The TIRS calibration plate heaters (two units connected in series) are powered ON/OFF, and they can provide up to 0.8W (12V/180Ω). In the case of the support plate heaters (two units connected in series with a total resistance of 180 Ω), the applied voltage is controlled to raise the temperature of the support plate by a certain ΔT above the value measured just before heating. To achieve the set point (ΔT), the electronic driver is commanded by a closed-loop digital control system implemented by software inside the ICU (Fig. 4).

The control system uses one of the two support plate Resistance Temperature Detectors (RTD) (either may be configured for this purpose) as a feedback sensor [5]. The electronic driver architecture is a 10-bit Power Wide Modulator (PWM), using a clock frequency of 10 kHz and driving voltage of 12V. The digital controller architecture is formed by an anti-windup Proportional-Integral digital controller (PI), followed by a discrete Infinite Impulse Response filter (IIR) and a gain block to tune the system response. The controller set-point is calculated from the temperature of the support plate before heating, $T_{ref} = T_{sp_initial} + \Delta T$.

On a practical level, the use of the heater of the support plate presents better performances than that of the calibration plate. The main reason is that the control system of the support plate eliminates the

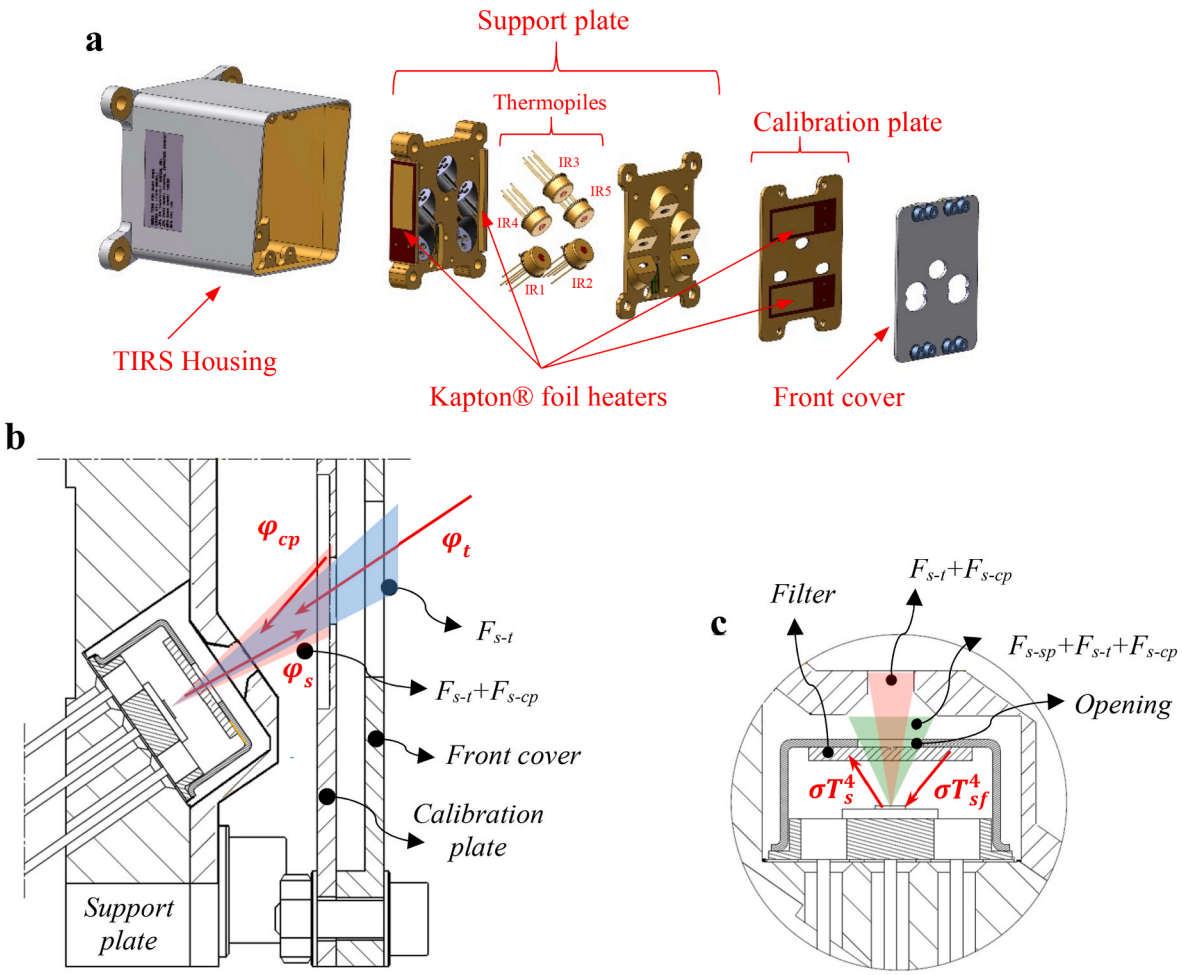


Fig. 3. Support and calibration plate subassemblies and their corresponding FoVs. (a) TIRS 3D exploded drawing, (b) 2D diagram of thermopile external view factors and fluxes (example for an upward-looking channel), (c) 2D diagram of internal fluxes and thermopile's filter accommodation.

temporal thermal gradients in the thermopiles through the control loop, thus minimizing the uncertainty associated with these gradients [14]. In addition, the heater power consumption is lower because the applied voltage is modulated, demanding <0.3 Wh versus 0.47 Wh for the calibration plate heater. Finally, flexibility, as it allows working with different set points above ambient (ΔT), to find a compromise between the power demanded and the settling time. For all these reasons, the calibration plate has been discarded for in-flight calibrations during the Mars operations, using only the support plate heating system.

3. In-flight calibration modeling

The TIRS mathematical model is shown in Eq. (1). The first term on the right-hand side (see Table 2 for the terminology) represents the net radiative flux exchange with the thermopile external elements, the target, and the calibration and support plates (Fig. 3a), calculated by integrating of Planck's law through their corresponding view factors. The second term on the right accounts for the thermopile package inner flux exchange (Fig. 3b), and it takes into account the effect of the package thermal gradients ($F_{sf} - F_s$), calculated using the Stefan-Boltzmann law since there is no filter limiting the bandpass of the fluxes inside the thermopile. The radiosities and the thermal gradient are calculated according to the equations described in Refs. [10,11].

The model includes a parameter called β to model the change in sensor global responsivity. It was defined under the assumption that dust deposition on the outer side of the thermopile filter through the opening would be the most likely cause of changes in the responsivity. Martian dust is opaque, has high emissivity, and reaches the same temperature as the thermopile package shortly after being deposited on the outer side of the filter, limiting its effective area (Fig. 3c). Thus, β represents the change in the thermopile external view factor ($F_{s-t} + F_{s-cp}$), taking a value between 1 (no degradation) and 0 (complete clogging).

The model originally presented in Ref. [1] assumed that the geometrical change of the viewing factors also modifies the modeling of the thermal gradients generated inside the thermopile. However, the analysis of the thermal calibration results shows that these gradients depend primarily on the thermal properties of the filter substrate material, and not on the external viewing factors [11]. Since the presence of dust does not modify the properties of the filters, nor their inward viewing factor, the original mathematical model in Eq. (18) of [1] has been modified, removing the parameter β from the second term on the right-hand side as shown in Eq. (1).

$$V_{out} = S(T_s)\cdot A_s\cdot\beta\cdot\left(F_{s-t}\cdot\varphi_t + F_{s-cp}\cdot\varphi_{cp} - \left(F_{s-t}+F_{s-cp}\right)\cdot\varphi_s\right) + S(T_s)\cdot A_s\cdot\left(1-F_{s-t}-F_{s-cp}-F_{s-sp}\right)\cdot\sigma\cdot\left(T_{sf}^4 - T_s^4\right) \quad (1)$$

3.1. In-flight calibration algorithm

The in-flight recalibration system uses a novel patent-protected al-

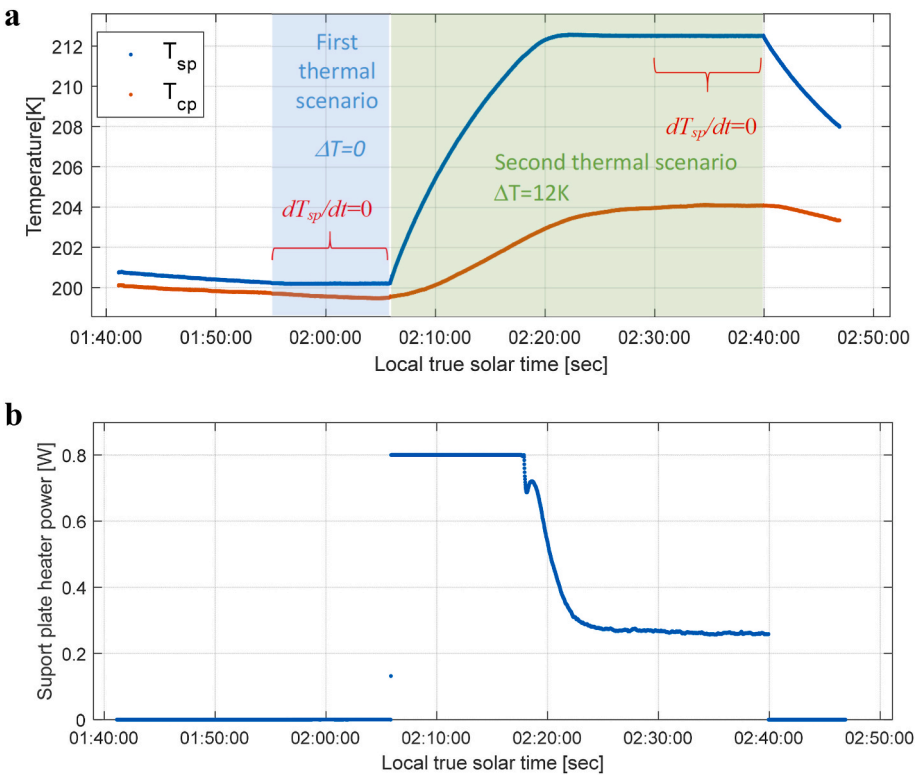


Fig. 4. In-flight calibration sequence of sol 722 at 2:00 h, using the support plate heater. **(a)** TIRS temperatures evolution. Shaded areas shows the temporal interval used for the calibration (radiative scenarios). **(b)** Evolution of heater power.

Table 2
Nomenclature.

Parameter	Description
V_{out}	thermopile output voltage, V
$S(T_s)$	thermopile responsivity versus temperature, V/W
A_s	thermopile detector area, m2
T_{cp}	calibration plate temperature, K
T_s	thermopile detector temperature (reference) equal to support plate temperature, K
T_{sp}	support plate temperature, K
T_{sf}	thermopile detector housing temperature (front part), K
F_{s-t}	thermopile detector-target view factor
F_{s-cp}	thermopile detector-calibration plate view factor
F_{s-sp}	thermopile detector-support plate view factor
β	change in sensor external view factor ($F_{s-t} + F_{s-cp}$)
φ_t	target radiosity (emitted plus reflected) inside channel spectrum, W/m^2
φ_{cp}	calibration plate radiosity (emitted plus reflected) inside channel spectrum, W/m^2
φ_s	thermopile detector radiosity (emitted plus reflected) inside channel spectrum, W/m^2
σ	Stefan-Boltzmann constant, W/m2· K^4
T_{sf}-T_s	thermopile's package thermal gradient, K
ΔT	support plate temperature gradient above the ambient during calibration, K
T_{ref}	set-point for the support plate controller, K

gorithm [15]. This algorithm compares the measurements from two different radiative scenarios: before and during the heating of the support plate (Fig. 4a). From this comparison, the value of the parameter β is estimated. In the first scenario, lasting 10 min, a temperature gradient of $\Delta T = 0\ K$ (setpoint $T_{ref} = T_{sp_initial}$) is established. This setpoint means that the heating power is meager, typically less than 1 mW, and that the $dT_{sp}/dt = 0$ condition is reached from the first second, minimizing the thermal gradients in the detectors [11]. In the second scenario, lasting 35 min, a temperature gradient of $\Delta T = 12\ K$ is established. Only the last 10 min are useful, during which $dT_{sp}/dt = 0$ (Fig. 4b).

Experimental data indicate that a higher value of ΔT during the heating of the support plate allows to reduce the uncertainty associated with the calibration process, as a consequence of a higher signal-to-noise ratio due to the higher change of the outgoing radiative flux from the detector (φ_s). The value of ΔT=12K has been selected as a compromise between the maximum achievable gradient and the required setting time.

One of the limitations of the system is that it can only be applied to those channels that operate in the thermal range, i.e., IR1, IR2, IR4 and IR5 (Table 1). The IR3 channel is only sensitive to the visible and near-infrared range, and therefore the 12K temperature increment of the support plate is not able to generate a change in the flux (φ_s) to have a signal-to-noise ratio large enough to perform its recalibration.

The algorithm uses Eq. (1), in which the degradation factor β and the irradiance of the target φ_t, are the unknowns. The rest of the variables and constants have been previously calibrated, knowing their value, or calculated from the RTDs and heater power measurements [10,11]. Using Eq. (1), a system of two linearly independent equations is built, as shown in Eqs. (2.1) and (2.2). Each equation corresponds to one of the irradiance scenarios, being linearly independent because of the change in the IR flux leaving the support plate. Both scenarios should be understood as the set of the 600 instantaneous samples taken every second, where $dT_{sp}/dt = 0$.

$$V_{out,\Delta T=0K}(i) = S\left(T_{s,\Delta T=0K}(i)\right)\cdot A_s\cdot\beta\cdot\left(F_{s-t}\cdot\varphi_{t,\Delta T=0K}(i)+F_{s-cp}\cdot\varphi_{cp,\Delta T=0K}(i)-\left(F_{s-t}+F_{s-cp}\right)\cdot\varphi_{s,\Delta T=0K}(i)\right)+S\left(T_{s,\Delta T=0K}(i)\right)\cdot A_s\cdot\left(1-F_{s-t}-F_{s-cp}-F_{s-sp}\right)\cdot\left(\sigma\cdot T^4_{sf,\Delta T=0K}(i)-\sigma\cdot T^4_{s,\Delta T=0K}(i)\right) \quad (2.1)$$

$$V_{out,\Delta T=12K}(i) = S\left(T_{s,\Delta T=12K}(i)\right)\cdot A_s\cdot\beta\cdot\left(F_{s-t}\cdot\varphi_{t,\Delta T=12K}(i)+F_{s-cp}\cdot\varphi_{cp,\Delta T=12K}(i)-\left(F_{s-t}+F_{s-cp}\right)\cdot\varphi_{s,\Delta T=12K}(i)\right)+S\left(T_{s,\Delta T=12K}(i)\right)\cdot A_s\cdot\left(1-F_{s-t}-F_{s-cp}-F_{s-sp}\right)\cdot\left(\sigma\cdot T^4_{sf,\Delta T=12K}(i)-\sigma\cdot T^4_{s,\Delta T=12K}(i)\right) \quad (2.2)$$

The algorithm's implemented solution uses the mean values of the target irradiances for each scenario, rather than the instantaneous values, Eq. (3). In this way, the undesirable effects of target irradiance fluctuations during the calibration are mitigated.

$$\overline{\varphi}_{t,\Delta T=0K}=\frac{1}{600}\sum_{i=1}^{600}\varphi_{t,\Delta T=0K}(i)\quad \overline{\varphi}_{t,\Delta T=12K}=\frac{1}{600}\sum_{i=1}^{600}\varphi_{t,\Delta T=12K}(i) \quad (3)$$

The system of equations Eq. (2) and Eq. (3) has three unknowns: β, which has a single value in both equations, and the two average target irradiances $\overline{\varphi}_{t,\Delta T=0K}$ and $\overline{\varphi}_{t,\Delta T=12K}$. It implies that we have an underdetermined system with multiple solutions. To solve it, it has to be transformed into an overdetermined system, assuming a relation between the target irradiances for the two radiative scenarios, thus reducing the irradiance to a single unknown. This is the main reason why the time of execution of the algorithm has been limited to nighttime hours (1:00 to 5:00). During this period there is a monotonic, almost linear evolution, and with less fluctuation in the irradiance of the target for all the channels [16].

To solve the system of equations for the optimal value of β, the algorithm follows an iterative procedure (Fig. 5). It starts from a $\beta = 1$ value, which indicates non-degraded responsivity. Then, its value is updated $\beta = \beta \pm \Delta\beta$ in each execution period to minimize certain error functions below a threshold.

The error functions are defined as the difference between the measured averaged irradiance, $\overline{\varphi}_t$, and the estimated irradiance, $\widehat{\varphi}_t$, for each scenario (Eq. (4)). In this way, two error functions can be defined for each irradiance scenario, Eqs. (4.1) and (4.2), and two solutions of β are obtained for each calibration dataset.

$$\widetilde{\varphi}_{t,\Delta T=12K}=\overline{\varphi}_{t,\Delta T=12K}-\widehat{\varphi}_{t,\Delta T=12K} \quad (4.1)$$

$$\widetilde{\varphi}_{t,\Delta T=0K}=\overline{\varphi}_{t,\Delta T=0K}-\widehat{\varphi}_{t,\Delta T=0K} \quad (4.2)$$

The estimated irradiances for each scenario are calculated from the measured irradiances for the other scenario. To do this a linear regression algorithm that extrapolates the results from one of the irradiance scenarios to the center of the other (the middle of the 10min) is used (Eqs. (5.1) and (5.2):

$$\widehat{\varphi}_{t,\Delta T=12K}=\widehat{\gamma}_{0,\Delta T=0K}+\widehat{\gamma}_{1,\Delta T=0K}\cdot i_{\Delta T=12K}$$
$$\left(\widehat{\gamma}_{0,\Delta T=0K},\widehat{\gamma}_{1,\Delta T=0K}\right)=LR\left(\varphi_{t,\Delta T=0K}(i)\right) \quad (5.1)$$

$$\widehat{\varphi}_{t,\Delta T=0K}=\widehat{\gamma}_{0,\Delta T=12K}+\widehat{\gamma}_{1,\Delta T=12K}\cdot i_{\Delta T=0K}$$
$$\left(\widehat{\gamma}_{0,\Delta T=12K},\widehat{\gamma}_{1,\Delta T=12K}\right)=LR\left(\varphi_{t,\Delta T=12K}(i)\right) \quad (5.2)$$

Fig. 6 shows the evolution (initial and final execution results) of the in-flight calibration algorithm for the IR1 channel with data from sol 722.

The following practical considerations about the implementation of the algorithm should be highlighted:

1) An increase in the value of β above 1 does not make physical sense because it would imply an improvement in the responsivity of the thermopiles, which is unlikely. However, due to fluctuations in the irradiance of the target during calibration, the algorithm occasionally yields β values > 1.
2) The value of $\Delta\beta$ ranges from 0.001 to 0.002 depending on the channel. These values are small enough to ensure a good resolution in the final value of β, while still ensuring the convergence of the algorithm and avoiding oscillations around the optimal value of β. Similarly, the thresholds applied to the error function as the algorithm stop condition, range from 0.2 to 0.01W/m^2 depending on the channel. These values were selected accounting for the absolute values of irradiance in each channel, the accuracy requirements, and the noise levels that affect the algorithm itself.
3) Particularly for channel IR2 (atmospheric temperature measurement at 40m height), the temperature estimator uses the slope of the

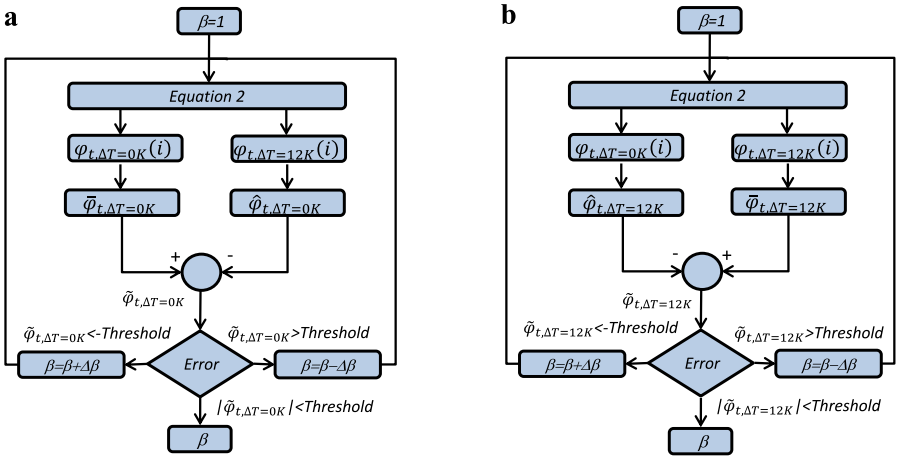


Fig. 5. Flowchart of the iterative in-flight calibration algorithm. **(a)** Error definition for the first scenario, $\Delta T = 0K$. **(b)** Error definition for the second scenario, $\Delta T = 12K$.

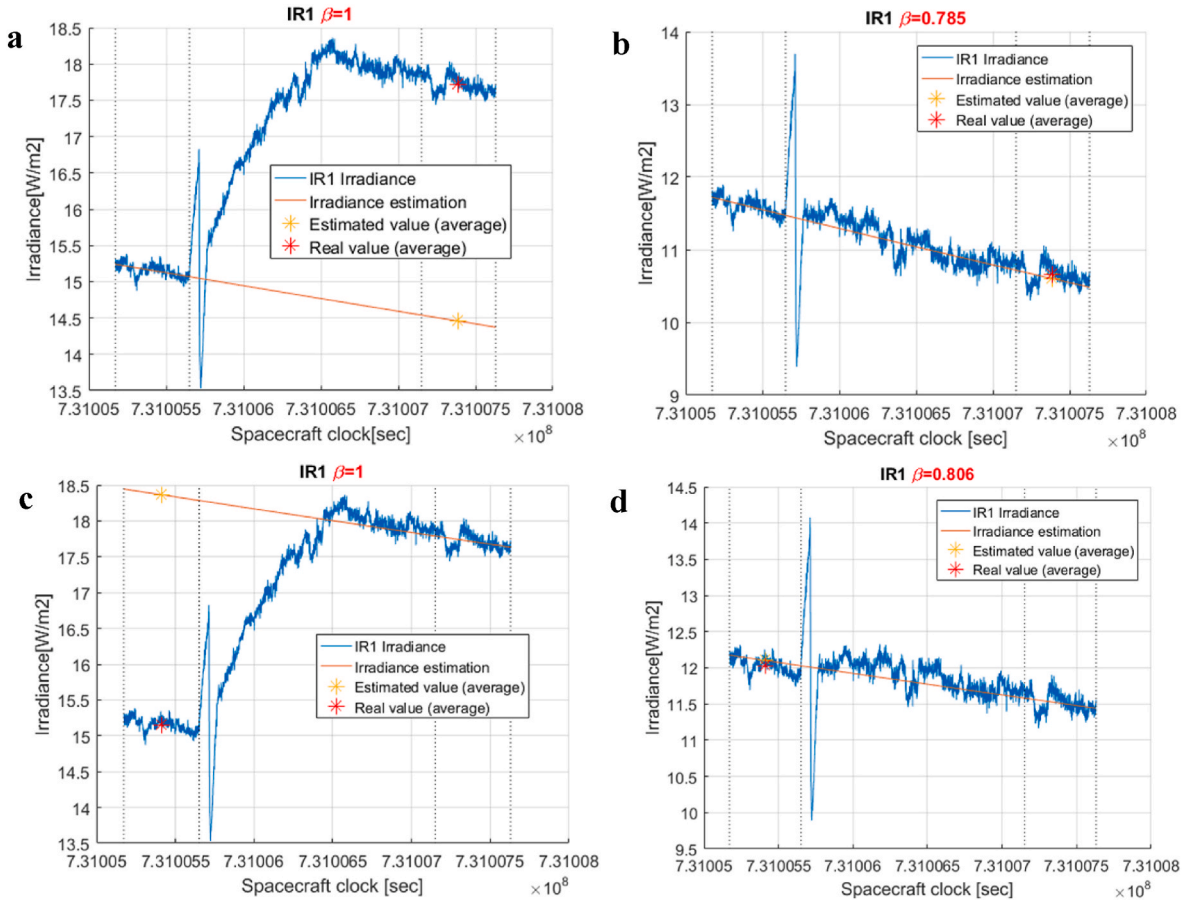


Fig. 6. Evolution of the measured irradiance for channel IR1 during the execution of the in-flight calibration algorithm for the second calibration dataset of sol 722 at 02:00. (a) Irradiance computed for the first iteration of the algorithm (β=*1*) using the error definition from Eq. (4.1). (b) Irradiance computed for the last iteration of the algorithm and final optimal value of β=*0.785* using the error definition from Eq. (4.1). (c) Irradiance calculated for the first iteration of the algorithm (β=*1*) using the error definition from Eq. (4.2). (d) Irradiance calculated for the last iteration of the algorithm and the final optimal value of β=*0.806*, using the error definition from Eq. (4.2).

Table 3
In-flight calibration campaigns.

Campaign (Sols)	Number of calibration sequences	ΔT (second scenario)
70–91	9	6K
159–171	6	12K
195–217	6	6K/12K
281–289	9	6K/9K/12K
331–334	4	12K
429–436	8	12K
503–506	8	12K
589–592	8	12K
643–646	8	12K
683–686	8	12K
718–722	8	12K
762–765	8	12K
796–799	8	12K

estimator ($\hat{\gamma}_1$) in Eq. (5) of channel IR5 (ground temperature). The atmospheric temperature is affected by a high variability during the algorithm execution time (45 min) [16], which leads to higher uncertainties in the linear estimation of the slope. This variability is significantly minimized in the regolith due to its greater thermal inertia [4], helping to minimize the uncertainty of the linear regression estimate. Therefore, it allows a better estimation of the temperature evolution trend for both the regolith and the atmosphere, since both variables share a similar tendency to decrease in an approximately linear fashion during the early morning and before sunrise [16].

4. In-flight calibration campaigns and analysis of the results

The result of β for each run of the algorithm is affected by the uncertainty associated with the linear estimator and the instabilities in the irradiance from the targets.

In addition, this uncertainty is different for each channel because the radiant flux emitted by the detector due to the heating of the support plate depends on the spectral range of the channel. The use of averages in the definition of the error functions allows us to mitigate the effects of these instabilities. To further reduce this effect, the results of eight runs of the algorithm with the two error definitions are used. Then, the 16 particular values are averaged to compute the best estimate of β. Ideally, the calibration data are taken during four consecutive sols, in which two calibrations are performed between 01:00 and 05:00 Local Mean Solar Time (LMST).

Table 3 shows a list of consecutive sols on which in-flight calibration campaigns have been performed, using the support plate heaters. Each calibration campaign results in a single estimate of the degradation factor β. For the first campaigns, it can be observed that the number of sols is different, as well as the temperature gradient ΔT. This is due to the testing and tuning phase of the algorithm.

Table 4 and Fig. 7 summarize the results of the different campaigns, giving a picture of the temporal evolution of the degradation for each channel during the mission.

Table 4
Results of the in-flight calibration campaigns. β represents the best-estimated value of the degradation. It is calculated as the mean of the degradations reported for each execution of the in-flight algorithm within a campaign. σ_β is the associated standard deviation.

Sol/ Channel	IR1 ($\beta \pm \sigma_\beta$)	IR2 ($\beta \pm \sigma_\beta$)	IR3 ($\beta \pm \sigma_\beta$)	IR4 ($\beta \pm \sigma_\beta$)	IR5 ($\beta \pm \sigma_\beta$)
70–91	0.870 ± 0.052	0.913 ± 0.100	0.969 ± 0.028	0.976 ± 0.021	0.947 ± 0.013
159–171	0.870 ± 0.052	0.872 ± 0.022	0.971 ± 0.018	0.985 ± 0.008	0.952 ± 0.006
195–217	0.887 ± 0.037	0.924 ± 0.092	0.967 ± 0.023	0.982 ± 0.012	0.950 ± 0.011
281–289	0.860 ± 0.047	0.872 ± 0.115	0.964 ± 0.027	0.965 ± 0.023	0.944 ± 0.013
331–334	0.868 ± 0.070	0.899 ± 0.050	0.972 ± 0.020	0.986 ± 0.010	0.958 ± 0.010
429–436	0.838 ± 0.032	0.844 ± 0.082	0.973 ± 0.023	0.984 ± 0.014	0.955 ± 0.010
503–506	0.845 ± 0.018	0.839 ± 0.054	0.967 ± 0.022	0.982 ± 0.012	0.949 ± 0.009
589–592	0.837 ± 0.019	0.789 ± 0.029	0.962 ± 0.015	0.977 ± 0.006	0.947 ± 0.005
643–646	0.824 ± 0.018	0.737 ± 0.075	0.961 ± 0.014	0.974 ± 0.006	0.946 ± 0.005
683–686	0.803 ± 0.038	0.698 ± 0.093	0.957 ± 0.023	0.965 ± 0.016	0.937 ± 0.010
718–722	0.808 ± 0.029	0.693 ± 0.040	0.962 ± 0.020	0.969 ± 0.014	0.941 ± 0.007
762–765	0.813 ± 0.023	0.707 ± 0.025	0.958 ± 0.019	0.969 ± 0.011	0.939 ± 0.007
796–799	0.804 ± 0.021	0.672 ± 0.037	0.945 ± 0.028	0.959 ± 0.017	0.930 ± 0.017

As previously noted, the IR3 channel cannot be calibrated by using the in-flight calibration system. The values provided for the degradation of channel IR3 are calculated from the values of channels IR4 and IR5, assuming that they have a similar degradation because they share the pointing angle. To calculate the degradation of this channel IR3 and the associated uncertainty, rectangular distribution functions were assumed for the data of the channels IR4 and IR5, where the extreme bound values are calculated as the maximum and minimum values for channels IR5 and IR4 plus ±2 times their standard deviations (95 % of confidence in a Gaussian distribution function), Eq. (6). Then, the value of β for IR3 corresponds to the average of these extreme values, and its standard deviation is equivalent to $1/(2\cdot\sqrt{3})$ of its difference, Eq. (6) [17].

$$\begin{aligned}\Delta_1 &= \max\{\beta_{IR4} + 2\cdot\sigma_{\beta IR4}\ ;\ \beta_{IR5} + 2\cdot\sigma_{\beta IR5}\}\\ \Delta_2 &= \min\{\beta_{IR4} - 2\cdot\sigma_{\beta IR4}\ ;\ \beta_{IR5} - 2\cdot\sigma_{\beta IR5}\}\\ \beta_{IR3} &= (\Delta_1 + \Delta_2)/2\\ \sigma_{\beta IR3} &= (\Delta_1 - \Delta_2)/(2\cdot\sqrt{3})\end{aligned} \quad (6)$$

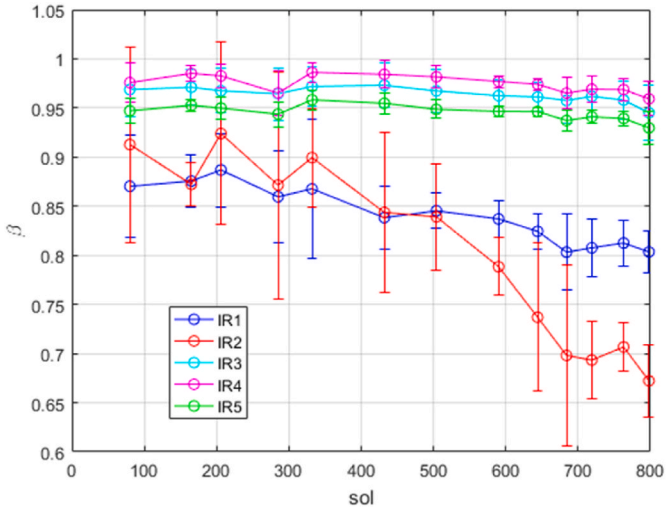


Fig. 7. Evolution of the parameter β during surface operations for the different in-flight calibration campaigns, the standard deviations (σ_β) are shown as error bars. The line plot represents the linear interpolation used for the β in between calibration campaigns.

From the experimentally determined values of the standard deviations, calculated for each calibration campaign, an overall uncertainty value of the flight calibration system can be estimated. This uncertainty can be expressed as a percentage, calculated as the root mean square of the sum of the uncertainties of the different campaigns $\sqrt{\sum \sigma_\beta/\beta}$. Table 5 summarizes the results for each channel.

The data provided in NASA's Planetary Data System (PDS) [18] use the degradations reported in this paper, using a linear interpolation for intermediate sols and extending the last calibrated value for the sols after the last calibration. The latter are corrected when a new value for the degradation is available and a new data reprocessing is performed before uploading to the PDS. The global uncertainties in Table 5 are also used to calculate the uncertainties reported in the PDS.

Fig. 8 shows the effect of the corrections applied to the different channels compared to the data without compensation for sol 762, as they appear in NASA's PDS in the "Calibrated Data" (CAL_TIRS file). The relevance of the corrections can be observed especially for the most degraded channels, IR1 and IR2.

4.1. Results analysis and discussion

The following conclusions can be drawn, given the experimental results of the thermopiles' responsivity and their evolution:

1. All TIRS channels present an initial degradation detected during the first calibration campaign at sols 70–91.
2. Channels with the same pointing angles, the IR1-IR2 and IR4-IR5 pairs, present similar initial degradations 10–13 % and 4–5% respectively. Moreover, this degradation is larger in those thermopiles oriented upwards IR1-IR2.
3. The initial degradation remains more or less constant (accounting for error bars) until sols 331–334. Then gradual degradation is observed from sols 429–436 to sols 683–686. The last three data for sols 718–722, 762–765, and 796–799 show stable results.
4. The increase in degradation for the IR2 channel (~20 %) is larger than for IR1 (~7 %), despite having the same orientation and similar initial degradation. In contrast, the IR4 and IR5 channels have similar degradation rates (~1–1.5 %).

From the analysis of these results, it can be concluded that the most likely cause of the decrease in responsivity is the deposition of dust on the thermopiles' filters. The reasons supporting this hypothesis are as follows:

1. The gradual and different degradation observed for each channel cannot be explained by the loss of hermeticity in the thermopiles' packages [7]. Such loss would have implied an almost instantaneous change of responsivity of about 30 %, associated with the replacement of the inner gas (krypton) by the Martian atmosphere, which has not been observed. In addition, this possibility

Table 5
Uncertainty of the in-flight calibration system uncertainty per channel. It is expressed as a percentage of β and calculated as the root mean square of the sum of the standard deviations of each campaigns.

Channel	IR1	IR2	IR3	IR4	IR5
β uncertainty	4.29 %	8.50 %	2.28 %	1.44 %	1.07 %

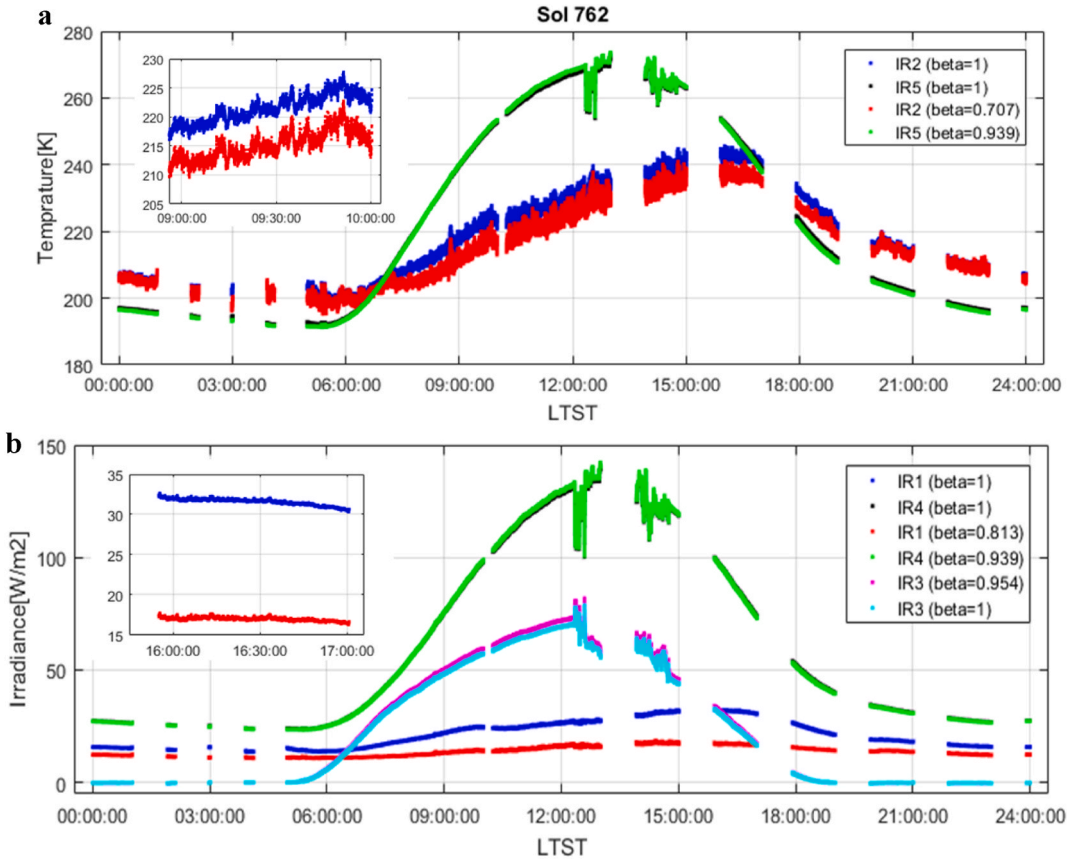


Fig. 8. Effect of in-flight calibration corrections, as reported in NASA's PDS "Calibrated Data" (CAL_TIRS file), versus the data without compensation for sol 762. a) Temperature channels (IR2 and IR5) and zoom for IR2 channel between ~9:00–10:00 (insert). b) Irradiance channels (IR1, IR3 and IR4) and zoom for IR1 channel between ~16:00–17:00 (insert).

is unlikely because the qualification of the thermopiles flight lot, Package Qualification and Validation [19], has demonstrated the reliability of the seal of all the units.

2. Gamma and neutron radiation may also be responsible for filters obscuration and as a result of the degradation of its transmittance. During cruise and surface operations thermopiles have been exposed to hard radiation. According to MEDA requirements, TIRS has to withstand (worst case) a total ionizing dose (gamma radiation) of 9.09 krads and a displacement damage dose (neutron radiation) of 1.78×10^{11} n/cm^2 equivalent to 1 MeV. As part of the qualification of the thermopiles, specific tests were performed on samples according to ESA SCC Basic specification 22900. The tests were passed without thermopiles degradation. Similar tests performed on quartz filter samples show minor changes in optical properties [20].
3. Another explanation for the decrease in global responsivity is the degradation of the transmittance of the thermopiles' filters [21] and/or the absorbance of the thermopiles' transducers [6], which could be caused by exposure to direct solar radiation. Depending on rover orientation and sun position, the optics of the upward-facing thermopiles may be exposed to direct solar radiation. Fig. 9a shows the number of hours per sol and the total cumulative hours in which this circumstance occurred. During the period of greatest responsivity degradation, sols 400 to 700, the number of exposure hours was among the lowest, which rules out this cause. As well as the fact that thermopiles looking downwards, and therefore not directly exposed to the sun, have also degraded.
4. An initial degradation is probably related to dust lifting from the surface during the landing caused by the retrorockets. During the landing and for the first two sols, the RSM (Remote Sensing Mast) of the rover, where the TIRS is accommodated, was folded on the rover deck with all TIRS channels facing upward and similarly exposed to the environment (Fig. 10a). Subsequently, on sol 2 the RSM rover was deployed (Fig. 10b), which probably removed some of the dust stuck to each channel unevenly, with those facing downward becoming cleaner.
5. The higher relative degradation of the upward-facing channels is likely justified because they are more exposed to dust deposition by gravitational sedimentation, the settling of particles on a fluid due to the effect of gravitational force. All in spite of the protection of some mechanical elements such as the sunshade, the front cover, and the calibration plate, which limit direct exposure to the environment, Fig. 10b (insert).
6. Optical sensors similar to the TIRS and with long operating times on the surface of Mars, such as the REMS-UV [22] or the MEDA-RDS and MEDA-Skycam [23], show similar and progressive degradations. Unlike REMS-UV [24] and MEDA-RDS [25], the TIRS does not include any dust-repellent elements such as powerful magnets [26], but it is protected from dust by mechanical elements and they are not looking upward vertically. A recent study reported the dust accumulation factors of the solar panels located in different Mars missions [27]. In the Insight mission, there was a loss of output power of 0.2 %/sun in the first 800 soles, a ratio similar to the TIRS results for the IR2 channel in the period 429–686. Like the results of Insight and contrary to those of Curiosity, Spirit, and Opportunity, TIRS has shown no signs of cleaning up to now and after more than a year on the surface of Mars.

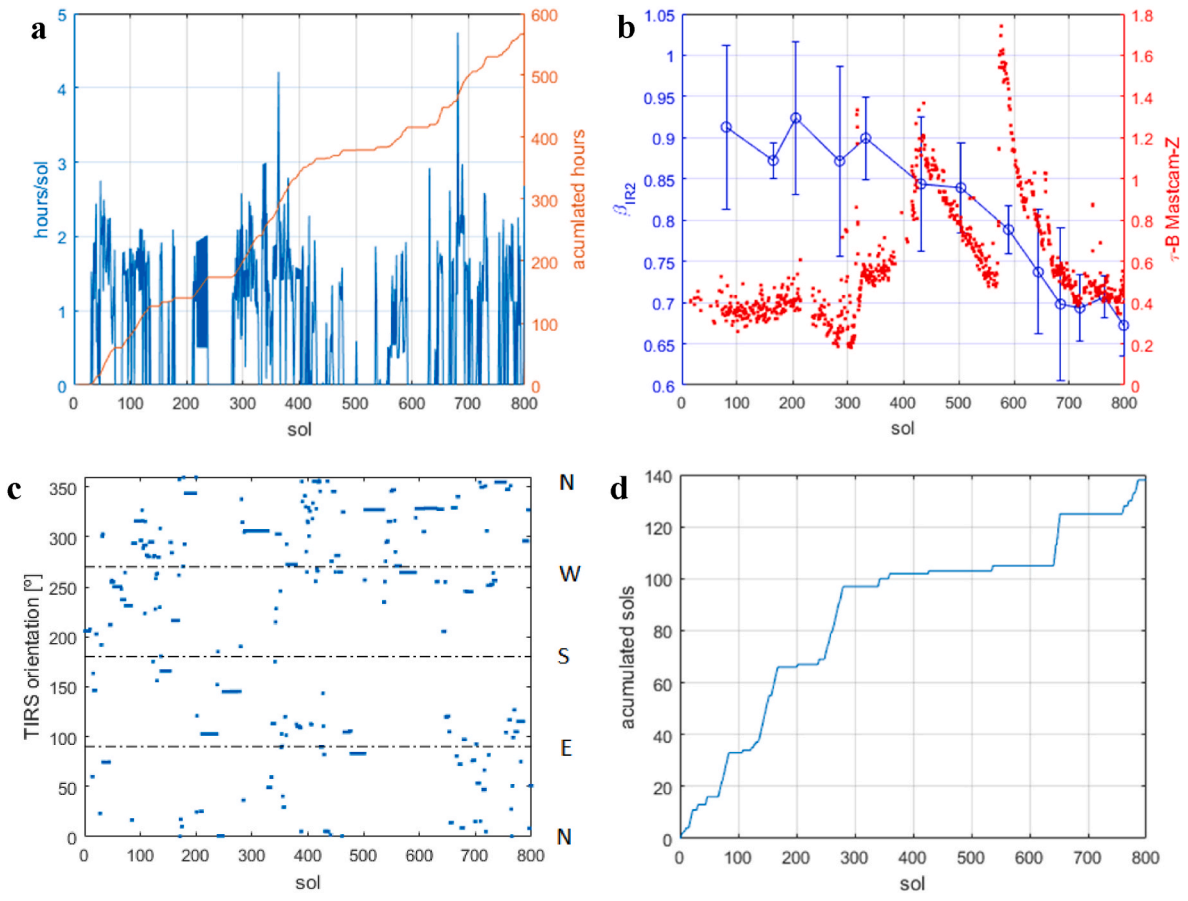


Fig. 9. a) Direct solar incidence on the thermopiles' FoV for the upward-looking channels (IR1 and IR2), (blue) solar exposure time per sol, (red) Cumulative exposure time. b) Evolution of the IR2 channel degradation and atmospheric opacity values at 480 nm measured by Mastcam-Z. c) Orientation of the TIRS when the rover was parked, (N) for North, (E) for East, (S) for South, and (W) for West. d) Number of cumulative sols where the rover orientation in the parking position is between 180 ± 65° (prevailing wind directions). (For interpretation of the references to colour in this figure legend, the reader is referred to the Web version of this article.)

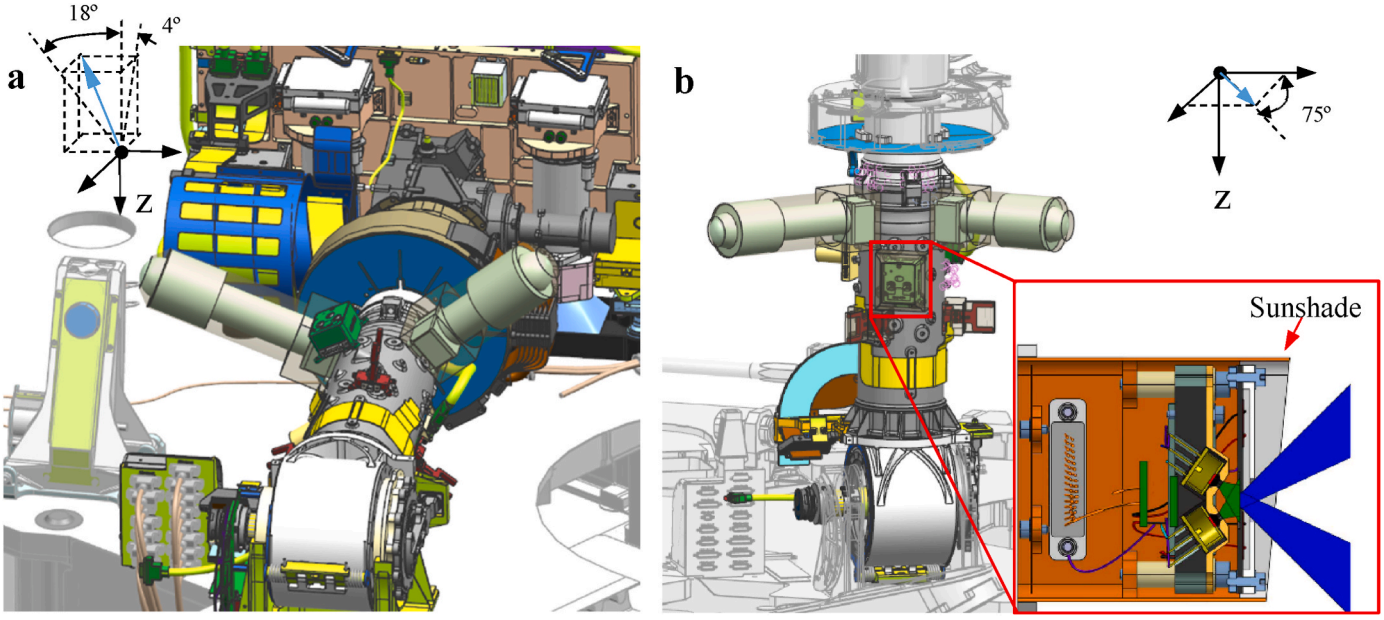


Fig. 10. TIRS pointing angle (front cover w.r.t. gravity vector 'z') and accommodation at rover RSM during Mars operations (credit NASA-JPL). (a) Before RSM deployment up to sol 2, (b) After RSM deployment from sol 2 onwards, (insert) FoV and protection elements (housing and front cover).

7. The increase in degradation from sol 400 coincides with a higher atmospheric opacity above 0.8 (dusty session), as does the stabilization from sol 700 with a return to low opacity values. In Fig. 9b, the degradation of the IR2 channel is superimposed with the opacity measured by the camera onboard Perseverance rover Mastcam-Z at 480 nm [28].
8. The greater degradation of responsivity, between sols 350–700, is not justified by greater exposure to the prevailing winds, which could blow up and accumulate dust from the ground on the detectors. The prevailing winds at Jezero, as measured by MEDA up to sol 250 [3] rotate throughout the day from the west (W) during nighttime to the east (E) in the afternoon, with a southward (S) component in between. Model simulations to estimate wind velocities and directions as a function of solar longitude confirm that the results measured by MEDA can extend beyond the first 250 sols, with small seasonal variations [29,30]. Most of the time between sols 400–630, the orientation of the TIRS was west (W) and northwest (NW) as shown in Fig. 9c and d, while the rover was at the parking position. It implies that except for the nighttime hours, when the wind speeds are below 3 m/s, the TIRS was shielded from the prevailing wind, thus not justifying the degradation. On the contrary, no degradation was observed for sols when the TIRS was exposed to the wind, as in between sols 130 and 275.
9. The seasonal evolution of vortices and dust devils measured by MEDA up to sol 420 is small, with a slight increase in activity around sol 350 [31]. In Ref. [32] it is shown that some dust-lifting events are correlated with dust devils. Although it is early to say this, because data on the activity of vortices and dust devils have not yet been published for the period of maximum degradation of the TIRS channels, there could be some correlation between the TIRS degradation up to sol 420 and the increase in dust devils activity from sol 350 onwards.
10. Channel IR2 shows a responsivity degradation ratio almost 3 times higher than IR1, ~20 % vs. ~7 % from the first calibration campaign to the last one. Both channels share the same pointing angle and a similar initial degradation. A hypothesis to explain this behavior could be the electromagnetic properties of the dust [26], and the electrical properties of the filter material on which the dust may be deposited. The base material for the filter of channel IR2 is germanium, while for channel IR1 is silicon [10]. Germanium has a relative dielectric constant (ε) of 15.8 versus 11.7 for silicon [33], which allows it to store more electrostatic charge and generate a higher electric field that may attract dust to its surface. A fact that supports this hypothesis, is that the IR4 and IR5 channels share the same type of filter base material, silicon, and the same pointing angle, reporting similar relative degradations throughout the mission ~1 % vs. 1.5 %.

Finally, the analyses performed here allow us to draw some conclusions regarding the design of radiometers similar to TIRS for future missions. The first would be to remove elements similar to the calibration plate that partially block the detectors' FoV, due to the improved performance of the calibration system that heats the detectors through a control algorithm that eliminates transient temperature gradients. Another possible improvement implemented in similar sensors [24,25] is the use of magnets to minimize dust deposition on the upward-facing channels. Despite being protected by mechanical elements, it has been shown that the upward-facing channels have degraded because of the electromagnetic properties of the dust [26] and the filters.

5. Conclusions

During the first 800 sols of MEDA on Mars, a total number of 13 in-flight calibration campaigns have been performed with the TIRS. Each campaign is nominally composed of 8 individual calibration sessions, performed on four consecutive sols, thus allowing the averaging to reduce the uncertainty associated with atmospheric variability during the calibration. The TIRS calibration system has shown its ability to estimate the degradation value of the responsivity of the IR detectors, using the support plate heater due to its better performance. The heating energy for each calibration session is below 0.3 Wh, and the overall uncertainty associated with the responsivity estimation for each campaign ranges from 1 % to 8.5 %, depending on the radiometer channel.

The different campaigns have made it possible to quantify the temporal evolution of the responsivity of the IR detectors throughout the mission for all the channels. In view of the results, the most likely cause of the degradation is dust deposition by gravitational sedimentation on the detector optics. Other causes such as a leak of the inner atmosphere of the thermopile packages or the degradation of the absorbance of the thermopile transducers have been discarded, as inconsistencies were found between the degradation hypotheses and the experimental data.

The initial degradation, reported from calibrations on sols 70–91, seems to be related to the rover's landing process and the exposure to the dusty atmosphere generated by the retro rockets. The pointing angle of the different channels conditions this initial degradation, which is determined by the effect of gravitational sedimentation and the deployment of the RSM on sol 2. Thus, the channels facing upwards IR1-IR2 show initial degradations between 10 and 13 %, and those facing downwards IR4-IR5 between 4 and 5%.

The gradual degradation experienced by all channels between sols 350 and 700 seems conditioned by the amount of dust in suspension in the atmosphere, coinciding with the seasonal period of highest atmospheric opacity. The channels looking upwards show higher additional degradations during this period, ~7 % for IR1 and ~20 % for IR2, than those looking downwards, between ~1–1.5 % for channels IR4 and IR5. The values for the upward looking channels are similar to those estimated for the MEDA RDS and SkyCam for this same period. The higher degradation rate of the IR2 channel compared to IR1, with which it shares the pointing angle, may be associated with the higher dielectric constant of the thermopile's filter material, Ge for IR2 versus Si for IR1, and therefore a higher capacity to accumulate electrostatic charge and to attract dust from the atmosphere. So far, no signs of cleaning up have been observed, after more than a year on the surface of Mars.

The data provided in the PDS for TIRS measurements account for the degradations reported in this paper, improving the accuracy of the data. In addition to that, the uncertainties of the in-flight calibration system are also considered in the calculation of the radiometer global uncertainties. Finally, the analyses and conclusions presented here may be useful and serve as a guide to improve the design of future radiometers for Mars missions.

Funding

This work has been funded by the Spanish *Ministry of Economy and Competitiveness*, through the projects No. ESP2014-54256-C4-1-R and AYA2015-65041-P; *Ministry of Science, Innovation and Universities*, projects No. ESP2016-79612-C3-1-R, ESP2016-80320-C2-1-R, RTI2018-098728-B-C31, RTI2018-099825-B-C31, MDM-2017-0737 and PID2021-126719OB-C41; *Instituto Nacional de Técnica Aeroespacial*; *Ministry of Science and Innovation's Centre for the Development of Industrial Technology*; Germán Martínez wants to acknowledge JPL funding from USRA Contract Number 1638782. The US co-authors performed their work under sponsorship from NASA's Mars 2020 project, from the Game Changing Development program within the Space Technology Mission Directorate and from the Human Exploration and Operations Directorate.

CRediT authorship contribution statement

Eduardo Sebastián: Writing – review & editing, Writing – original

draft, Visualization, Validation, Methodology, Investigation, Formal analysis, Data curation, Conceptualization. **Germán Martínez:** Writing – review & editing, Validation, Investigation, Funding acquisition, Data curation. **Miguel Ramos:** Writing – review & editing, Investigation, Data curation. **Michael D. Smith:** Writing – review & editing, Validation, Investigation, Data curation. **Verónica Peinado:** Software, Resources, Investigation, Data curation. **Luis Mora:** Software, Resources, Investigation, Data curation. **Mark T. Lemmon:** Resources, Investigation. **Álvaro de Vicente-Retortillo:** Validation, Resources, Investigation, Data curation. **Javier de Lucas:** Writing – review & editing, Methodology, Formal analysis. **Ricardo Ferrándiz:** Visualization, Resources. **José A. Rodríguez-Manfredi:** Project administration, Investigation, Funding acquisition.

Declaration of competing interest

The authors declare that they have no known competing financial interests or personal relationships that could have appeared to influence the work reported in this paper.

Acknowledgment

This work forms part of the research project on the design and scientific issues of the NASA MARS2020 MEDA. A special thanks to all MEDA Co-Is and collaborators, who participated in a variety of ways in the development of MEDA TIRS, as well as reviewers for their contributions to the improvement of the article.

References

[1] J.A. Rodriguez-Manfredi, A. Alonso, V. Apestigue, I. Arruego, D. Banfield, J. Boland, J. Ceballos, A. Cobos, P. Conrad, E. Cordoba, T. del Rio, M. Dominguez-Pumar, S. Espejo, A. Fernandez, R. Ferrandiz, E. Fischer, M. Genzer, J. Gomez-Elvira, F. Gomez-Gomez, A.-M. Harri, C. Hernandez, M. Hieta, R. Hueso, J. J. Jimenez, V. Jimenez, A. Larman, A. Lepinette, M. Lemmon, S. Madsen, T. Mäkinen, M. Marin, J. Martín Soler, G.M. Martínez, A. Molina, L. Mora, J. Moreno, S. Navarro, C.E. Newman, C. Ortega, V. Peinado, A. Peña, I. Perez-Grande, S. Perez-Hoyos, J. Pla, J. Polkko, O. Prieto, M. Ramos, J. Romeral, A. Saiz-Lopez, A. Sanchez-Lavega, I. Sard, J.T. Schofield, E. Sebastian, M.D. Smith, R. E. Sullivan, L.K. Tamppari, A. Thomson, F. Torrero, J. Torres, R. Urqui, T. Velasco, D. Viudez-Moreiras, M. de la Torre Juarez, MEDA, the Mars environmental dynamics analyzer, A suite of sensors for the Mars 2020 mission, Space Sci. Rev (2020), https://doi.org/10.1007/s11214-021-00816-9.

[2] K.A. Farley, K.H. Williford, K.M. Stack, R. Bhartia, A. Chen, M. de la Torre-Juarez, K. Hand, Y. Goreva, C.D.K. Herd, R. Hueso, Y. Liu, J.N. Maki, G.M. Martínez, R. C. Moeller, A. Nelessen, C.E. Newman, D. Nunes, A. Ponce, N. Spanovich, P. A. Willis, L.W. Beegle, J.F. Bell III, A.J. Brown, S.-E. Hamran, J.A. Hurowitz, S. Maurice, D.A. Paige, J.A. Rodriguez-Manfredi, M. Schulte, R.C. Wiens, Mars, 2020 mission overview, Space Sci. Rev. 216 (2020).

[3] J.A. Rodriguez-Manfredi, M. de la Torre Juarez, A. Sanchez-Lavega, R. Hueso, G. Martinez, M.T. Lemmon, C.E. Newman, A. Munguira, M. Hieta, L.K. Tamppari, J. Polkko, D. Toledo, E. Sebastian, M.D. Smith, I. Jaakonaho, M. Genzer, A. De Vicente-Retortillo, D. Viudez-Moreiras, M. Ramos, A. Saiz-Lopez, A. Lepinette, M. Wolff, R.J. Sullivan, J. Gomez-Elvira, V. Apestigue, P.G. Conrad, T. Del Rio-Gaztelurrutia, N. Murdoch, I. Arruego, D. Banfield, J. Boland, A.J. Brown, J. Ceballos, M. Dominguez-Pumar, S. Espejo, A.G. Fairén, R. Ferrandiz, E. Fischer, M. Garcia-Villadangos, S. Gimenez, F. Gomez-Gomez, S.D. Guzewich, A.-M. Harri, J.J. Jimenez, V. Jimenez, T. Makinen, M. Marin, C. Martin, J. Martin-Soler, A. Molina, L. Mora-Sotomayor, S. Navarro, V. Peinado, I. Perez-Grande, J. Pla-Garcia, M. Postigo, O. Prieto-Ballesteros, S.C.R. Rafkin, M.I. Richardson, J. Romeral, C. Romero, H. Savijarvi, J.T. Schofield, J. Torres, R. Urqui, S. Zurita, The MEDA team, the diverse meteorology of Jezero crater over the first 250 sols of Perseverance on Mars, Nat. Geosci. (2023), https://doi.org/10.1038/s41561-022-01084-0.

[4] G.M. Martínez, E. Sebastián, A. Vicente-Retortillo, M.D. Smith, J.R. Johnson, E. Fischer, H. Savijärvi, D. Toledo, R. Hueso, L. Mora-Sotomayor, H. Gillespie, A. Munguira, A. Sánchez-Lavega, M.T. Lemmon, F. Gómez, J. Polkko, L. Mandon, V. Apéstigue, I. Arruego, M. Ramos, P. Conrad, C.E. Newman, M. de la Torre-Juarez, F. Jordan, L.K. Tamppari, T.H. McConnochie, A.-M. Harri, M. Genzer, M. Hieta, M.-P. Zorzano, M. Siegler, O. Prieto, A. Molina, J.A. Rodríguez-Manfredi, Surface energy budget, albedo and thermal inertia at Jezero Crater, Mars, as observed from the Mars 2020 MEDA instrument, J. Geophys. Res.: Planets 128 (2023) e2022JE007537, https://doi.org/10.1029/2022JE007537.

[5] J. Pérez-Izquierdo, E. Sebastián, G. Martínez, A. Bravo, M. Ramos, J.A. Rodríguez Manfredi, The thermal infrared sensor (TIRS) of the mars environmental dynamics analyzer (MEDA) instrument onboard mars 2020, a general description and performance analysis, Measurement 122 (2018) 432–442, https://doi.org/10.1016/j.measurement.2017.12.004.

[6] A. Ihring, U. Dillner, E. Kessler, Thermopile infrared sensor with precisely patterned high-temperature resistant black absorber layer, Proceedings OPTO 2009 & IRS2 (2009) 197–202, https://doi.org/10.5162/irs09/i1.3.

[7] T. Elbel, S. Poser, H. Fischer, Thermoelectric radiation microsensors, Sensor Actuator Phys. 42 (1994) 80040–80045, https://doi.org/10.1016/0924-4247(94,1–3.

[8] E. Sebastián, C. Armiens, J. Gómez-Elvira, M.P. Zorzano, J. Martinez-Frias, B. Esteban, M. Ramos, The rover environmental monitoring station ground temperature sensor: a pyrometer for measuring ground temperature on mars, Sensors 10 (10) (2010) 9211–9231, https://doi.org/10.3390/s101009211.

[9] N.T. Mueller, J. Knollenberg, M. Grott, E. Kopp, I. Walter, C. Krause, et al., Calibration of the HP3 radiometer on InSight, Earth Space Sci. 7 (2020) e2020EA001086, https://doi.org/10.1029/2020EA001086.

[10] E. Sebastian, G.M. Martínez, M. Ramos, F. Haenschke, R. Ferrándiz, M. Fernández, J.A. Rodriguez Manfredi, Radiometric and angular calibration tests for the MEDA-TIRS radiometer onboard NASA's Mars 2020 mission, Measurement 164 (2020) 107968, https://doi.org/10.1016/j.measurement.2020.107968.

[11] E. Sebastián, G. Martínez, M. Ramos, I. Pérez-Grande, J. Sobrado, J.A. Rodríguez Manfredi, Thermal calibration of the MEDA-TIRS radiometer onboard NASA's Perseverance rover, Acta Astronaut. 182 (2021) 144–159, https://doi.org/10.1016/j.actaastro.2021.02.006.

[12] T. Spohn, K. Seiferlin, A. Hagermann, J. Knollenberg, A.J. Ball, M. Banaszkiewicz, J. Benkhoff, S. Gadomski, W. Gregorczyk, J. Grygorczuk, M. Hlond, G. Kargl, E. Kuhrt, N. Kömle, J. Krasowski, W. Marc, J.C. Zarnecki, Mupus – a thermal and mechanical properties probe for the Rosetta lander Philae, Space Sci. Rev. 128 (2007) 339, https://doi.org/10.1007/s11214-006-9081-2.

[13] T. Spohn, M. Grott, S.E. Smrekar, J. Knollenberg, T.L. Hudson, C. Krause, N.Müller, J. Jänchen, A. Börner, T. Wippermann, O. Krömer, R. Lichtenheldt, L. Wisniewski, J. Grygorczuk, M. Fittock, S. Rheershemius, T. Spröwitz, E. Kopp, I.Walter, A.C. Plesa, D. Breuer, P. Morgan, W.B. Banerdt, the heat flow and physical properties package (HP 3) for the InSight mission, Space Sci. Rev. 214 (2018) 96, https://doi.org/10.1007/s11214-018-0531-4.

[14] E. Sebastián, C. Armiens, J. Gómez-Elvira, Infrared temperature measurement uncertainty for unchopped thermopile in presence of case thermal gradients, Infrared Phys, Technol. 54 (2011) 75–83, https://doi.org/10.1016/j.infrared.2010.12.038.

[15] E. Sebastián Martínez, C. Armiens Aparicio, J. Gómez-Elvira Rodríguez, R. Ferrándiz Guibelalde, Medidor infrarrojo autocalibrable y procedimiento de autocalibración de dicho medido (Spain Patent No. 2 539 408), Oficina Española de Patentes y Marcas (2015). https://patentimages.storage.googleapis.com/07/f2/40/2eefff375d960f/ES2539408A1.pdf.

[16] A. Munguira, R. Hueso, A. Sánchez-Lavega, M. de la Torre-Juarez, G.M. Martínez, C.E. Newman, E. Sebastian, A. Lepinette, A. Vicente-Retortillo, B. Chide, M. T. Lemmon, T. Bertrand, R.D. Lorenz, D. Banfield, J. Gómez-Elvira, J. Martín-Soler, S. Navarro, J. Pla-García, J.A. Rodríguez-Manfredi, J. Romeral, M.D. Smith, J. Torres, Near surface atmospheric temperatures at Jezero from Mars 2020 MEDA measurements, J. Geophys. Res.: Planets 128 (2023), https://doi.org/10.1029/2022JE007559.

[17] Bipm, Iec, Ifcc, Iso, Iupac, Iupap, OIML; BIPM Joint committee for guides in metrology, Evaluation of Measurement Data Guide to the Expression of Uncertainty in Measurement JCGM 100 (2008) 2008 (GUM 1995 with Minor Corrections), 1st ed.; BIPM: Sèvres,France.

[18] Manuel de la Torre Juarez, Jose A. Rodriguez-Manfredi, Mars 2020 MEDA bundle, NASA Planetary Data System (2021), https://doi.org/10.17189/1522849.

[19] R. Ramesham, Extreme temperature thermal cycling tests and results to assess reliability for Mars rover flight qualification. Proceedings of the Microelectronics Reliability and Qualification Workshop, USA, Manhattan Beach, CA, February 2004, pp. 3–4.

[20] J.R Denison, J.L. Prebola, A.Evans, D. Fullmer, J.L. Hodges, D.H. Crider, D.S. Crews. "Comparison of flight and ground tests of environmental degradation of MISSE-6 SUSpECS materials" Proceedings of the 11th Spacecraft Charging Technology Conference – 2010.

[21] J. Schmidt, Light-induced degradation in crystalline silicon solar cells, Diffus. Defect Data, Pt. B: Solid State Phenom. 95 (187) (2003), https://doi.org/10.4028/www.scientific.net/SSP.95-96.187.

[22] A. Vicente-Retortillo, G.M. Martínez, N. Renno, C.E. Newman, I. Ordonez-Etxeberria, M.T. Lemmon, M.I. Richardson, R. Hueso, A. Sánchez-Lavega, Seasonal deposition and lifting of dust on Mars as observed by the 527 Curiosity rover, Sci. Rep. 8 (1) (2018) 1–8.

[23] A. Vicente-Retortillo, M.T. Lemmon, G.M. Martinez, D. Toledo, V. Apestigue, I. Arruego, J.A. Rodriguez-Manfredi, Dust accumulation from MEDA measurements at Jezero crater, in: Mars. 54th Lunar and Planetary Science Conference 2023 (LPI Contrib. No. 2806), 2023.

[24] J. Gómez-Elvira, C. Armiens, L. Castañer, M. Domínguez, M. Genzer, F. Gómez, R. Haberle, A.-M. Harri, V. Jiménez, H. Kahanpää, L. Kowalski, A. Lepinette, J. Martín, J. Martínez-Frías, I. McEwan, L. Mora, J. Moreno, S. Navarro, M.A. de Pablo, V. Peinado, A. Peña, J. Polkko, M. Ramos, N.O. Renno, J. Ricart, M. Richardson, J. Rodríguez-Manfredi, J. Romeral, E. Sebastián, J. Serrano, M. de la Torre Juárez, J. Torres, F. Torrero, R. Urquí, L. Vázquez, T. Velasco, J. Verdasca, M.-P. Zorzano & J. Martín-Torres, REMS: The Environmental Sensor Suite for the Mars Science Laboratory Rover. Space Sci Rev 170 (2012) 583–640, https://doi.org/10.1007/s11214-012-9921-1.

[25] V. Apestigue, A. Gonzalo, J.J. Jiménez, J. Boland, M. Lemmon, de J.R. Mingo, E. García-Menendez, J. Rivas, J. Azcue, L. Bastide, et al., Radiation and dust sensor

for mars environmental dynamic analyzer onboard M2020 rover, Sensors 22 (8) (2022) 2907, https://doi.org/10.3390/s22082907.

[26] J.F. Bell, H.Y. McSween, J.A. Crisp, R.V. Morris, S.L. Murchie, N.T. Bridges, J. R. Johnson, D.T. Britt, M.P. Golombek, H.J. Moore, A. Ghosh, J.L. Bishop, R. C. Anderson, J. Brückner, T. Economou, J.P. Greenwood, H.P. Gunnlaugsson, R. M. Hargraves, S. Hviid, J.M. Knudsen, M.B. Madsen, R. Reid, R. Rieder, L. Soderblom, Mineralogic and compositional properties of martian soil and dust: results from mars pathfinder, J. Geophys. Res. 105 (E1) (2000) 1721–1755, https://doi.org/10.1029/1999JE001060.

[27] R.D. Lorenz, G.M. Martínez, A. Spiga, A. Vicente-Retortillo, C.E. Newman, N. Murdoch, F. Forget, E. Millour, T. Pierron, Lander and rover histories of dust accumulation on and removal from solar arrays on Mars, Planet, Space Sci 207 (2021) 105337, https://doi.org/10.1016/j.pss.2021.105337.

[28] J.F. Bell, J.N. Maki, G.L. Mehall, M.A. Ravine, M.A. Caplinger, Z.J. Bailey, S. Brylow, J.A. Schaffner, K.M. Kinch, M.B. Madsen, A. Winhold, A.G. Hayes, P. Corlies, C. Tate, M. Barrington, E. Cisneros, E. Jensen, K. Paris, K. Crawford, C. Rojas, L. Mehall, J. Joseph, J.B. Proton, N. Cluff, M.J. Wolff, et al., The mars 2020 perseverance rover Mast camera zoom (Mastcam-Z) multispectral, stereoscopic imaging investigation, Space Sci. Rev. 217 (2021) 24, https://doi.org/10.1007/s11214-020-00755-x.

[29] C.E. Newman, M. de la Torre Juárez, J. Pla-García, R.J. Wilson, S.R. Lewis, L. Neary, M.A. Kahre, F. Forget, A. Spiga, M.I. Richardson, F. Daerden, T. Bertrand, D. Viúdez-Moreiras, R. Sullivan, A. Sánchez-Lavega, B. Chide, J.A. Rodriguez-Manfredi, Multi-model meteorological and aeolian predictions for Mars 2020 and the Jezero crater region, Space Sci. Rev. 217 (2021) 20.

[30] J. Pla-García, S.C.R. Rafkin, G.M. Martinez, Á. Vicente-Retortillo, C. E. Newman, H. Savijärvi, M. de la Torre, J. A. Rodriguez-Manfredi, F. Gómez, A. Molina, D. Viúdez-Moreiras, A. M. Harri, Meteorological predictions for Mars 2020 Perseverance Rover landing site at Jezero crater, Space Sci. Rev. 216 (2020) 148.

[31] R. Hueso, C.E. Newman, T. del Río-Gaztelurrutia, A. Munguira, A. Sánchez-Lavega, D. Toledo, V. Apéstigue, I. Arruego, A. Vicente-Retortillo, G. Martínez, M. Lemmon, R. Lorenz, M. Richardson, D. Viudez-Moreiras, M. de la Torre-Juarez, J. A. Rodríguez-Manfredi, L.K. Tamppari, N. Murdoch, S. Navarro-López, J. Gómez-Elvira, M. Baker, J. Pla-García, A.M. Harri, M. Hieta, M. Genzer, J. Polkko, I. Jaakonaho, T. Makinen, A. Stott, D. Mimoun, B. Chide, E. Sebastian, D. Banfield, A. Lepinette-Malvite, Convective vortices and dust devils detected and characterized by Mars 2020, J. Geophys. Res.: Planets 128 (2023) e2022JE007516, https://doi.org/10.1029/2022JE007516.

[32] A. Vicente-Retortillo, G. M. Martínez, M. T. Lemmon, R. Hueso, J. R. Johnson, R. Sullivan, C. E. Newman, E. Sebastián, D. Toledo, V. Apéstigue, I. Arruego, A. Munguira, A. Sánchez-Lavega, N. Murdoch, M. Gillier, A. Stott, L. Mora-Sotomayor, T. Bertrand, L. K. Tamppari, M. de la Torre Juárez, J.-A. Rodríguez-Manfredi, Dust lifting through surface albedo changes at Jezero Crater, Mars, J. Geophys. Res.: Planets 128 (2023) e2022JE007672, doi:10.1029/2022JE007672.

[33] W.C. Dunlap, R.L. Watters, Direct measurement of the dielectric constants of silicon and germanium, Phys. Rev. 92 (1396) (1953), https://doi.org/10.1103/PhysRev.92.1396.